No-Load Magnetic Field and Cogging Force Calculation in LPMSMs with Semi-Closed Slots

H. Z. Hu, J. Zhao, X. D. Liu, ***Y. G. Guo***, and J. G. Zhu

***Abstract*—This paper presents an improved analytical subdomain model for predicting the magnetic field in linear permanent magnet synchronous machines (LPMSMs) with semi-closed slots accounting for the finite length of primary iron core and secondary back-iron. The whole field domain is divided into eight subdomains and the magnetic field in each subdomain is solved by applying the variable separation method, adequate boundary conditions and interface conditions. In this model, both the slot and end effects are considered. The thrust and normal forces are calculated by the Maxwell stress theory. The finite element analysis is carried out to validate the analytical model. Finally, an LPMSM prototype is manufactured and tested. The experimental results show that the developed analytical model has high accuracy for predicting the magnetic field and forces.**

***Index Terms*—Linear PM machines, improved analytical model, slot effect, end effect.**

I. Introduction

LINEAR permanent magnet (PM) synchronous machines (LPMSMs) can provide direct thrust force without the need of conversion from rotational torque to linear force, and thus are increasingly employed in various industrial and military applications, such as railway transportation, robotic systems and electromagnetic launchers [1-5]. Among various types of LPMSMs, the slotted topologies suffer from the slot and end effects which increase the thrust fluctuation and decrease the machine controllability. In the design and optimization of an LPMSM, accurate prediction of the magnetic field is critical for the performance analysis and evaluation. Owing to various advantages, the analytical method is still preferred for the initial design and optimization, although the widely used numerical methods can easily take into account the complicated geometry and iron saturation. The analytical method has been widely applied in the field analysis of LPMSMs, such as LPMSMs with the slot and end effects neglected [6-9], and coreless LPMSMs [10], [11]. However, when the slot and end effects must be considered, the analytical modeling becomes rather complicated.

The slot and end effects of LPMSMs can be accounted for by the magnetic equivalent circuit (MEC) which is widely used due to its simplicity and fast computation [12-17]. In [13], a relatively simple and accurate MEC model is proposed for LPMSMs and the air gap flux density distribution is obtained by linear interpolation of flux densities at specific mover positions. In [15], an MEC model corrected by the axisymmetric 2D finite element method (FEM) and experimental characterization is presented to completely characterize a small linear PM oscillatory motor. The precision of the magnetic circuit parameters is improved through numerical iterations. However, for the MEC method, the reluctances for different flux paths should be preliminarily known and the field distribution is only calculated at a few discrete points, resulting in inaccurate force calculation.

The Schwarz-Christoffel (SC) conformal mapping can consider the slot and end effects by transforming a complex structure into a relatively simple one, in which the analytical field solution can be readily obtained [1], [18-20]. In [1] and [18], the magnetic field distribution of LPMSMs is predicted by the subdomain (SD) method, i.e. the whole field domain is firstly divided into a few subdomains with adequate boundary and interface conditions, and then the field in each subdomain is solved analytically. The slot effects are accounted for by introducing a relative permeance function obtained by the SC mapping. However, the end effects are neglected by assuming that the machine is infinitely long. In [19], to reduce the computing time, a model of one pole-pair with slots while neglecting the end effects is analyzed by the SC mapping method. The slotted model with n vertices in the W-domain is directly transformed to a rectangle with n vertices in the Z-domain in which the magnetic field is calculated. In [20], the method of [19] is applied to an LPMSM accounting for both the slot and end effects. The complicated conformal mapping is completed by the MATLAB SC Toolbox.

The SD method is an elegant way for analytical determination of magnetic fields in electrical machines [21-24]. In [21], a tubular LPMSM is assumed to be infinitely long and comprised of an infinite number of finite-length armatures. The magnetic field is calculated in three regions, viz., the PMs, the air-gap and the space between adjacent armatures. This model, however, neglects the slot and the secondary end effects. In [22] and [23], under the assumption that the length of iron core is infinite, a general framework is proposed for calculating the open circuit and armature reaction magnetic field distribution of slotted tubular LPMSMs. In [24], to consider the end effects, an enlarged slot is added to the end of iron yoke and then periodic boundary is imposed. This method, however, can only consider approximately the end effects of the primary iron yoke, while the end effects of the secondary back-iron are ignored.

This paper presents an improved SD model with both the slot and end effects for predicting the magnetic field distribution and cogging force. The LPMSM in Cartesian coordinates is firstly transformed into an arc-segment PMSM in polar

coordinates. The analytical field expression of each subdomain is obtained by the variable separation method and the coefficients in the field expressions are determined by applying the boundary and interface conditions. The thrust and normal forces are then calculated. The magnetic field and forces calculated by the analytical model are compared with those obtained by the FEM. A prototype LPMSM is fabricated and tested. The experimental results agree well with those predicted by the analytical model.

II. Model of Linear PMSM

The structure diagram of an LPMSM is shown in Fig. 1. Fig. 2(a) shows the corresponding 2D model. The parameters in the figure are: the length of the primary iron, L_s, the height of the primary iron, h_s, the length of the secondary back-iron, L_r, the end length of the secondary back-iron, L_e, the height of the secondary back-iron, h_r, pole pitch, L_p, the width of PMs, L_m, the height of the PMs, h_m, the length of air-gap, g, the depth of the slots, h_c, the width of slots, L_w, the height of slot-opening, h_0, the width of slot opening, b_0, and the slot pitch, L_c. From the 2D model in the Cartesian coordinates, it can be seen that to consider the primary and secondary end effects, the magnetic field should be divided into 12 subdomains: 1, 2-1, 2-2, 3-1, …, 6, 7j and 8i (i, j=1,2,…,N_s), where N_s is the number of slots. The left subdomains 2-1, 3-1, and 5-1 extend to the left boundary x=-∞ and the right subdomains 2-2, 3-3, and 5-2 to the right boundary x=+∞. The modeling of PM should be conducted only in subdomain 3-2. The separation of subdomains 2, 3 and 5 will significantly increase the boundary and interface conditions, which make the field calculation very complicated.

In order to reduce the complexity, an approximate 2D analytical model is proposed and shown in Fig. 2(b). To obtain this model, the LPMSM is firstly deflexed to connect the left and the right boundaries of x=-∞ and x=+∞, and then subdomains 2-1 and 2-2, 3-1, 3-2 and 3-3, 5-1 and 5-2 are combined to form subdomains 2, 3, 5, respectively. Finally, the LPMSM in the Cartesian coordinates is converted to an arc-segment PMSM in the polar coordinates with the radius of curvature r→+∞. Theoretically, the two models in the Cartesian and polar coordinates are equivalent due to r→+∞. Practically, the model in the polar coordinates becomes unrealistic when r→+∞. If the radius of curvature r is assumed to be a finite value, the model will become an approximate model because of the curvature effect, which can be reduced by increasing the radius of the model.

In the approximate 2D model, the secondary back-iron and PMs are converted to the arc secondary, and the primary iron is converted to the arc primary. The magnetization direction of PMs is changed from the y-direction in the Cartesian coordinates to the radial direction in the polar coordinates. Compared with the 2D model in the Cartesian coordinates, the number of subdomains in the approximate 2D model is reduced from 12 to 8. The parameters in the analytical model are: inner radius of primary iron, R_s, outer radius of primary iron, R_{so}, radius of slot top, R_{sa}, radius of slot bottom, R_{sb}, outer radius of PM, R_m, outer radius of secondary back-iron, R_r, inner radius of secondary back-iron, R_r, span angle of primary iron, θ_1, span angle of Region 5, θ_2, span angle of secondary back-iron, θ_3, span angle of Region 2, θ_4, pole pitch, θ_p, span angle of PM, θ_m, slot pitch, θ_c, span angle of slot, θ_w, span angle of slot-opening, θ_{b0}, and length of air-gap, g. To ensure that the magnetic field of slotted LPMSM can be precisely calculated, the parameters of the analytical model should be properly chosen.

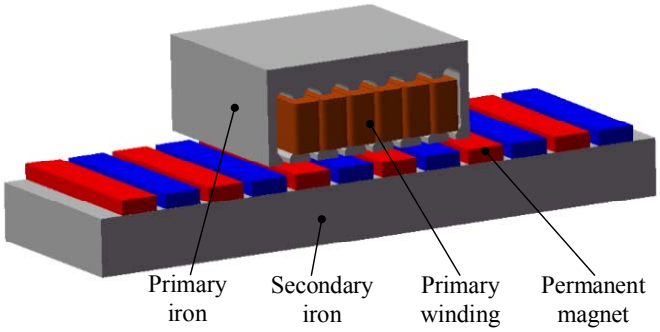

Fig. 1 Structure diagram of the LPMSM.

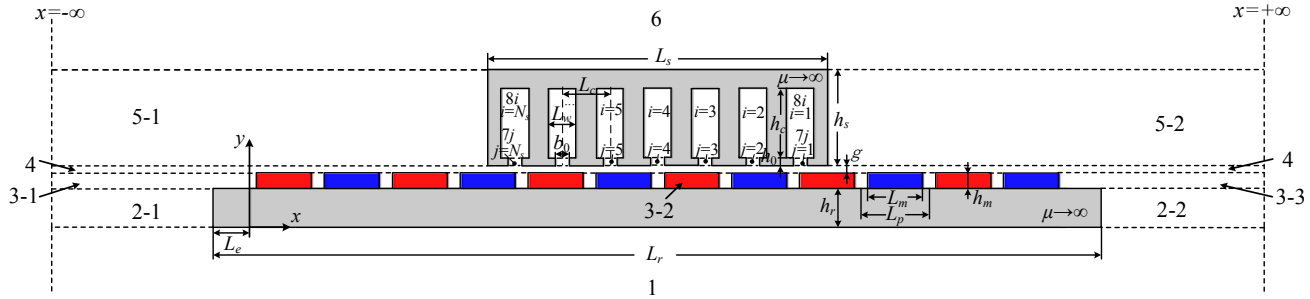

(a)

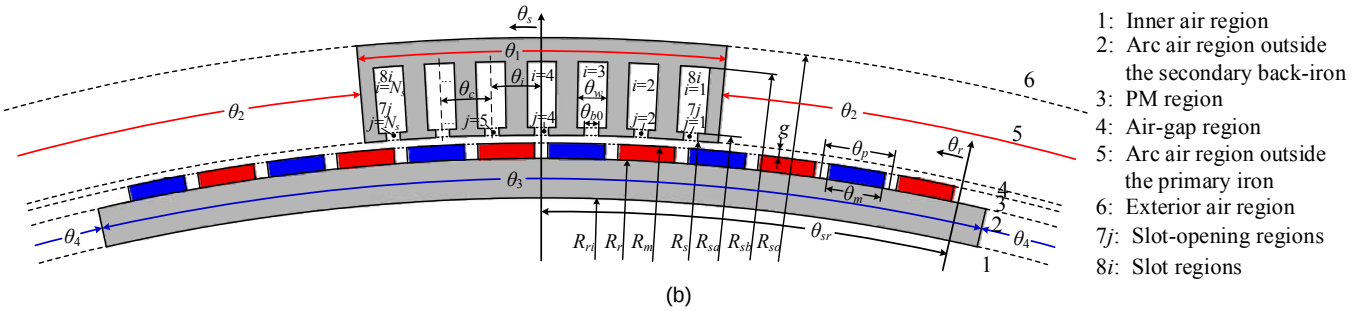

Fig. 2. Models of the LPMSM with semi-closed slots: (a) 2D model; and (b) approximate 2D model.

In the LPMSM, the position relationship between the primary iron and PMs, and the air-gap length are sensitive parameters, and they should remain unchanged. Hence, the R_m, θ_1, and θ_3 are firstly determined by:

$$R_m = \frac{L_{re}}{2\pi} \tag{1}$$

$$\theta_1 = \frac{L_s}{L_{re}} \times 2\pi \tag{2}$$

$$\theta_3 = \frac{L_r}{L_{re}} \times 2\pi \tag{3}$$

where L_{re} is the circumference of the outer surface of PMs in the approximate analytical model. Then, the other parameters can be obtained as

$$R_s = R_m + g \tag{4}$$

$$R_{so} = R_m + g + h_s \tag{5}$$

$$R_{sa} = R_m + g + h_0 \tag{6}$$

$$R_{sb} = R_m + g + h_0 + h_c \tag{7}$$

$$R_r = R_m - h_m \tag{8}$$

$$R_{ri} = R_m - h_m - h_r \tag{9}$$

$$\theta_{b0} = \frac{b_0}{L_{re}} \times 2\pi \tag{10}$$

$$\theta_c = \frac{L_w}{L_{re}} \times 2\pi \tag{11}$$

$$\theta_p = \frac{L_p}{L_{re}} \times 2\pi \tag{12}$$

$$\theta_m = \frac{L_m}{L_{re}} \times 2\pi \tag{13}$$

III. Analytical Solution of Magnetic Field

In this paper, the following assumptions are made to enable and simplify the analytical solution: (a) The permeability of the primary iron and the secondary back-iron is infinite; (b) The axial end effect is negligible; and (c) The permeability of gaps between magnets is assumed to be equal to that of PMs.

A. Model of the PMs

For the approximate 2D model shown in Fig. 2(b), θ_s is the mechanical angular position in the arc primary reference frame (θ_s=0 refers to the center of the arc primary) and θ_r is the mechanical angular position in the arc secondary reference frame (θ_r=0 is the beginning of the PMs when the pole arc to pole pitch ratio α_p=1). If the translation velocity of LPMSM is v_s and the rotation speed of the approximate 2D model is ω_r, the relationship between v_s and ω_r is

$$\omega_r = \theta_p \times \frac{v_s}{L_p} \tag{14}$$

The transformation between the arc primary and secondary reference frames is $\theta_s=\theta_r+\theta_{sr}$, where the angle difference $\theta_{sr}=\omega_r t+\theta_0$, and θ_0 is the initial position.

In the polar coordinates, the magnetization vector $\vec{M}$ of a PM can be given by

$$\vec{M} = M_r \vec{e}_r + M_\theta \vec{e}_\theta \tag{15}$$

where M_r is the radial component of the magnetization vector, M_θ the tangential component, and $\vec{e}_r$ and $\vec{e}_\theta$ are the radial and tangential unit vectors, respectively. For the radial magnetization, the tangential component of the magnetization vector is zero. The radial component is shown in Fig. 3. It can be seen that the span angle of all PMs is $N_p\theta_p$ instead of 2π, where N_p is the number of PMs. This is mainly due to that the PM arrangement does not occupy the whole region 3 as shown in Fig. 2(b).

The radial and tangential components of the magnetization $\vec{M}$ can be represented in the arc primary reference frame as

$$M_r(\theta_s) = \sum_{n=1}^{\infty} M_{rcn}\cos(n\theta_s) + M_{rsn}\sin(n\theta_s) \tag{16}$$

$$M_\theta(\theta_s) = \sum_{n=1}^{\infty} M_{\theta cn}\cos(n\theta_s) + M_{\theta sn}\sin(n\theta_s) \tag{17}$$

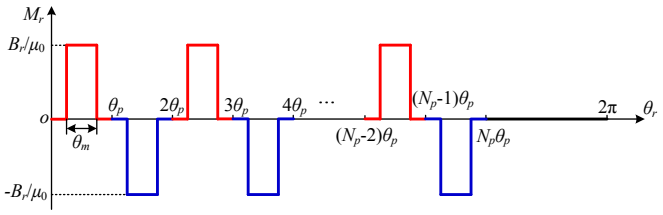

Fig. 3. Waveforms of the radial components of PM magnetization.

B. Governing Partial Differential Equations

As shown in Fig. 2(b), the field domain is divided into eight subdomains: Region 1 is the inner air region; Region 2 is the arc air region outside the secondary back-iron; Region 3 is the PM region; Region 4 is the air-gap region; Region 5 is the arc air region outside the primary iron; Region 6 is the exterior air region; Region 7j (j=1,2,…,N_s) is the slot-opening region; and Region 8i (i=1,2,…,N_s) is the slot region.

To describe the magnetic flux density $\vec{B}$, the magnetic vector potential $\vec{A}$ is introduced. For the 2D case in polar coordinates, the magnetic vector potential reduces to its axial component A_z. According to the Maxwell's equations, the magnetic vector potential is governed by the Poisson equation in the PM region and Laplace equation in other Regions, i.e.,

$$\frac{\partial^2 A_z}{\partial r^2}+\frac{1}{r}\frac{\partial A_z}{\partial r}+\frac{1}{r^2}\frac{\partial^2 A_z}{\partial \theta^2}=\begin{cases}-\dfrac{\mu_0}{r}\left(M_\theta-\dfrac{\partial M_r}{\partial \theta}\right) & \text{in Region 3}\\ 0 & \text{in Regions } \{1,2,4,5,6,7j,8i\}\end{cases} \tag{18}$$

By using the variable separation method, the general solutions of the vector potential in different subdomains can be expressed as the following [25]:

In region 1,

$$A_{1z}=\sum_{n=1}^{\infty}A_{1n}f_{1an}(r)\cos(n\theta_s)+C_{1n}f_{1an}(r)\sin(n\theta_s) \tag{19}$$

where $f_{1an}(r)=\left(\dfrac{r}{R_{ri}}\right)^n$.

In region 2,

$$A_{2z}=\sum_{m=1}^{\infty}\left[A_{2m}f_{2am}(r)+B_{2m}f_{2bm}(r)\right]\cos\frac{m\pi}{\theta_4}(\theta_s-\theta_{sr}-\theta_3) \tag{20}$$

where $f_{2am}(r)=\left(\dfrac{r}{R_r}\right)^{\frac{m\pi}{\theta_4}}$ and $f_{2bm}(r)=\left(\dfrac{r}{R_{ri}}\right)^{-\frac{m\pi}{\theta_4}}$.

In region 3,

$$\begin{aligned}A_{3z}&=A_p(r,\theta_s)+\sum_{n=1}^{\infty}\left[A_{3n}f_{3an}(r)+B_{3n}f_{3bn}(r)\right]\cos(n\theta_s)\\&\quad+\left[C_{3n}f_{3an}(r)+D_{3n}f_{3bn}(r)\right]\sin(n\theta_s)\end{aligned} \tag{21}$$

where $A_p(r,\theta_s)$ is a particular solution of Poisson equation,

$$A_p(r,\theta_s)=\sum_{n=1}^{\infty}l_{cn}(r)\cos(n\theta_s)+l_{sn}(r)\sin(n\theta_s)$$

$$l_{cn}(r)=\begin{cases}\dfrac{\mu_0(M_{c\theta n}-nM_{srn})}{n^2-1}r & n\neq 1\\ -\dfrac{\mu_0(M_{c\theta n}-M_{srn})}{2}r\ln r & n=1\end{cases}$$

$$l_{sn}(r)=\begin{cases}\dfrac{\mu_0(M_{s\theta n}+nM_{crn})}{n^2-1}r & n\neq 1\\ -\dfrac{\mu_0(M_{s\theta n}+M_{crn})}{2}r\ln r & n=1\end{cases}$$

$f_{3an}(r)=\left(\dfrac{r}{R_m}\right)^n$, and $f_{3bn}(r)=\left(\dfrac{r}{R_r}\right)^{-n}$.

In region 4,

$$\begin{aligned}A_{4z}&=\sum_{n=1}^{\infty}\left[A_{4n}f_{4an}(r)+B_{4n}f_{4bn}(r)\right]\cos(n\theta_s)\\&\quad+\left[C_{4n}f_{4an}(r)+D_{4n}f_{4bn}(r)\right]\sin(n\theta_s)\end{aligned} \tag{22}$$

where $f_{4an}(r)=\left(\dfrac{r}{R_s}\right)^n$, and $f_{4bn}(r)=\left(\dfrac{r}{R_m}\right)^{-n}$.

In region 5,

$$A_{5z}=\sum_{k=1}^{\infty}\left[A_{5k}f_{5ak}(r)+B_{5k}f_{5bk}(r)\right]\cos\frac{k\pi}{\theta_2}\left(\theta_s+\frac{\theta_2}{2}-\pi\right) \tag{23}$$

where $f_{5ak}(r)=\left(\dfrac{r}{R_{so}}\right)^{\frac{k\pi}{\theta_2}}$, and $f_{5bk}(r)=\left(\dfrac{r}{R_s}\right)^{-\frac{k\pi}{\theta_2}}$.

In region 6,

$$A_{6z}=\sum_{n=1}^{\infty}B_{6n}f_{6bn}(r)\cos(n\theta_s)+D_{6n}f_{6bn}(r)\sin(n\theta_s) \tag{24}$$

where $f_{6bn}(r)=\left(\dfrac{r}{R_{so}}\right)^{-n}$.

In region 7j,

$$A_{7jz}=\sum_{u=1}^{\infty}\left[A_{7ju}f_{7au}(r)+B_{7ju}f_{7bu}(r)\right]\times\cos\frac{u\pi}{\theta_{b0}}\left(\theta_s+\frac{\theta_{b0}}{2}-\theta_j\right) \tag{25}$$

where $f_{7au}(r)=\left(\dfrac{r}{R_{sa}}\right)^{\frac{u\pi}{\theta_{b0}}}$, and $f_{7bu}(r)=\left(\dfrac{r}{R_s}\right)^{-\frac{u\pi}{\theta_{b0}}}$.

In region 8i,

$$A_{8iz}=\sum_{v=1}^{\infty}B_{8iv}f_{8av}(r)\times\cos\frac{v\pi}{\theta_w}\left(\theta_s+\frac{\theta_w}{2}-\theta_i\right) \tag{26}$$

where $f_{8av}(r)=\left(\dfrac{R_{sa}}{R_{sb}}\right)^{\frac{v\pi}{\theta_w}}\left(\dfrac{r}{R_{sb}}\right)^{\frac{v\pi}{\theta_w}}+\left(\dfrac{r}{R_{sa}}\right)^{-\frac{v\pi}{\theta_w}}$.

C. Determination of Integration Constants

The field solution of the whole domain can be obtained by joining these general solutions of subdomains by applying the boundary conditions and interface conditions between subdomains, which are defined by the continuity of the radial flux density B_r and the tangential field strength H_θ.

The magnetic flux density and the magnetic field strength can be obtained from the vector potential by

$$B_r=\frac{1}{r}\frac{\partial A_z}{\partial \theta} \tag{27}$$

$$B_\theta=-\frac{\partial A_z}{\partial r} \tag{28}$$

$$H_r=\begin{cases}\dfrac{1}{\mu_0\mu_r r}\dfrac{\partial A_z}{\partial \theta}-\dfrac{1}{\mu_r}M_r & \text{in Region 3}\\ \dfrac{1}{\mu_0 r}\dfrac{\partial A_z}{\partial \theta} & \text{in Regions } \{1,2,4,5,6,7j,8i\}\end{cases} \tag{29}$$

$$H_\theta=\begin{cases}-\dfrac{1}{\mu_0\mu_r}\dfrac{\partial A_z}{\partial r}-\dfrac{1}{\mu_r}M_\theta & \text{in Region 3}\\ -\dfrac{1}{\mu_0}\dfrac{\partial A_z}{\partial r} & \text{in Regions } \{1,2,4,5,6,7j,8i\}\end{cases} \tag{30}$$

By applying the interface conditions, the unknown integration constants can be obtained. The detailed derivation process is shown in the Appendix.

IV. Force Calculation

According to the Maxwell stress theory, the force on a rigid body placed in an electromagnetic field can be calculated. The force acting on the primary iron is equal to that acting on the secondary back-iron and PMs except that their directions are opposite to each other. Hence, in this paper, a cylindrical enclosed surface which is located in Region 4 is selected as the integration surface, as shown in Fig. 4.

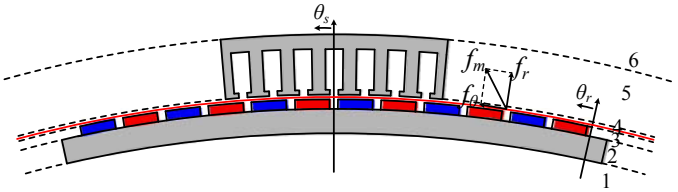

Fig. 4. The magnetic stress vector and its components in polar coordinates.

The magnetic stress vector on the enclosed surface is given by [26-27]

$$\vec{f}_m = \frac{1}{\mu_0}\left(B_r^2 - \frac{1}{2}\left|\vec{B}\right|^2\right)\vec{e}_r + \frac{1}{\mu_0}B_r B_\theta \vec{e}_\theta \tag{31}$$

There are two components in the magnetic stress vector. One component is the radial component f_r which can be used to approximate the normal force, that is, the y-direction force in the actual LPMSM, and the other is the tangential component f_θ which can be used to approximate the thrust force, that is, the x-direction force in the actual LPMSM. If the magnetic field is assumed uniform in the axial direction, the surface integration becomes a line integral multiplied by the axial length of iron core. The radial and tangential forces in the integral form can be written as

$$\vec{F}_r = \frac{1}{2\mu_0}L_1\int_0^{2\pi}\left[B_{r2}^2(r,\theta) - B_{\theta 2}^2(r,\theta)\right]rd\theta \tag{32}$$

$$\vec{F}_\theta = \frac{1}{\mu_0}L_1\int_0^{2\pi}B_{r2}(r,\theta)B_{\theta 2}(r,\theta)rd\theta \tag{33}$$

where L_1 is the axial length, r the radius of the integration surface, and B_{r2} and $B_{\theta 2}$ are the radial and tangential components of the flux density at radius r, respectively.

V. Validation by FEM and Experiment

To verify the analytical model, the linear FEM is applied to an LPMSM with semi-closed slots with the main parameters as shown in Table I. Based on the previous analysis in Section II, the corresponding parameters in the analytical model with the circumference of the PM outer surface L_{re} = 500 mm are shown in Table II.

Fig. 5 shows the FEM predicted flux density distributions when the primary iron is located at the middle and the end positions, respectively. Figs. 6-10 show the comparison between the analytical and FEM predictions of the normal and tangential flux density distributions in the air-gap, PM, slot opening, and slot regions when the primary iron is located at the middle and the end positions. It can be seen that the subdomain model accounting for the slot and end effects has an accuracy comparable to the FEM prediction for the flux density in the PM, air-gap, and slot opening regions. A small discrepancy in the slot region may be attributed to the meshing in the FEM model since the flux density in the slot region is very small.

Fig. 11 compares the thrust and normal forces of the LPMSM with semi-closed slots predicted by the analytical model and FEM. The analytical prediction of the thrust force agrees well with that obtained by the FEM, while the normal force prediction between the analytical model and FEM shows some discrepancy. The maximum error is less than 2%. This may be attributed to the curvature effect of the analytical model, and the discretization effects of the FEM. It is noted that the force calculation is relatively sensitive to the accuracy of the magnetic field solution, and thus, attention must be paid to the accuracy of the flux density components in both the analytical and FEM calculations. In this regard, the finite element mesh must be relatively fine in the air-gap region. While for the analytical prediction, the virtual length L_{re} must be sufficiently long, that is, the curvature of analytical model must be small enough to avoid higher harmonic terms. On the other hand, both finer meshes and higher harmonic terms increase the computation time.

To validate the analytical and FEM results, a prototype of LPMSM with semi-closed slots is manufactured and tested. Fig. 12 shows a photo of the experiment platform. The thrust is measured by a force sensor with the fullscale of 98N and precision of 0.2%. The relative position between the primary iron and secondary back-iron is measured by a vernier caliper with precision of 0.02mm.

Because of the diversity and assembling tolerance, the actual width of each PM varies from 9.99mm to 10.01mm, and the total length of 20 PMs is about 200.62mm, which is 0.6mm longer than the design. On the other hand, the magnetic nonlinearity of the iron cores could yield certain discrepancy between the theoretical and experimental results. To eliminate the error caused by these factors, the width of PMs in the analytical model and FEM model is adjusted to the average value of 10.03mm and the nonlinear FEM is employed to recalculate the field and thrust force.

TABLE I
Parameters of LPMSM

Parameter	Value	Parameter	Value
Length of primary iron, L_s	64.8mm	Pole arc to pole pitch ratio, α_p	1.0
Height of primary iron, h_s	26mm	Number of slots, N_s	7
Length of secondary iron, L_r	210mm	Width of slot, L_w	4.5mm
Height of secondary iron, h_r	15mm	Depth of slot, h_c	13mm
Length of the end of secondary iron, L_e	5mm	Width of slot-opening, b_0	2mm
Axial length, L_1	50mm	Height of slot-opening, h_0	1mm
Length of air-gap, g	1mm	Slot pitch, L_c	8.33mm
Number of PMs, N_p	20	PM remanence, B_r	1.27T
Pole pitch, L_p	10mm	Relative permeability, μ_r	1.043
Width of PM, L_m	10mm	Magnetization	Parallel
Thickness of PM, h_m	4mm		

TABLE II
Corresponding Parameters in Analytical Model of LPMSM

Parameter	Value	Parameter	Value
Extended length, L_{re}	500mm	Number of PMs, N_p	20
Outer radius of PM, R_m	79.58mm	Pole pitch, θ_p	7.20deg
Span angle of primary iron, θ_1	46.66deg	Span angle of PM, θ_m	7.20deg
Span angle of secondary iron, θ_3	151.20deg	Pole arc to pole pitch ratio, α_p	1.0
Inner radius of primary iron, R_s	80.58mm	Number of slots, N_s	7

Outer radius of primary iron, R_{so}	106.58mm	Width of slot, θ_w	3.24deg
Outer radius of secondary iron, R_r	75.58mm	Width of slot-opening, θ_{b0}	1.44deg
Inner radius of primary iron, R_{ri}	60.58mm	Slot pitch, θ_c	6.00deg
Radius of slot top, R_{sa}	81.58mm	PM remanence, B_r	1.27T
Radius of slot bottom, R_{sb}	94.58mm	Relative permeability, μ_r	1.043
Axial length, L_1	50mm	Magnetization	Radial

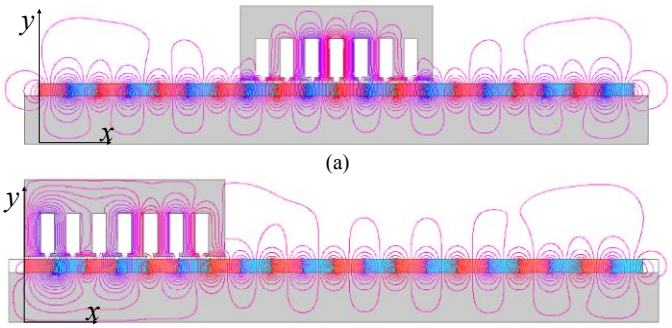

Fig. 5. FEM predicted flux-lines distribution with different relative positions of primary iron and PMs: (a) middle position, and (b) end position.

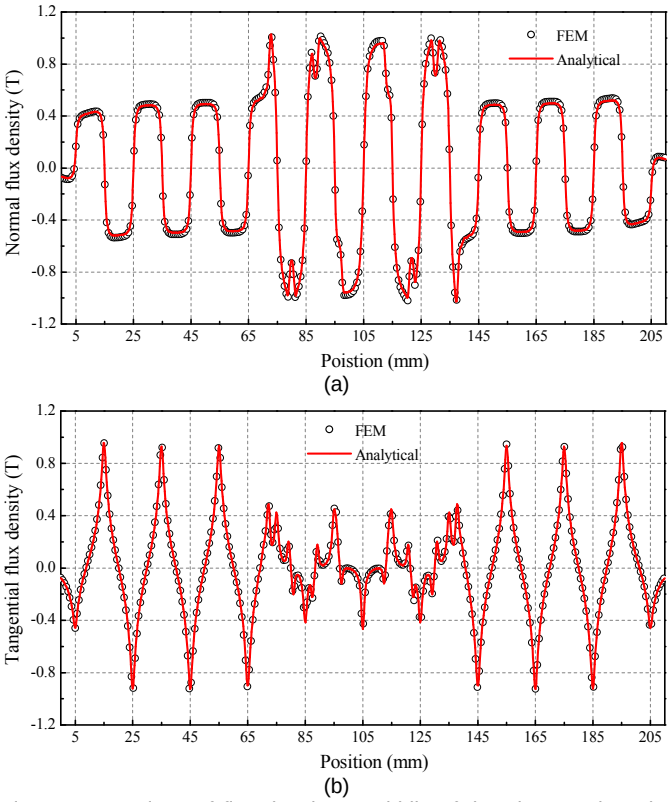

Fig. 6. Comparison of flux density at middle of the air gap when the primary iron is at the middle position: (a) normal flux density; and (b) tangential flux density.

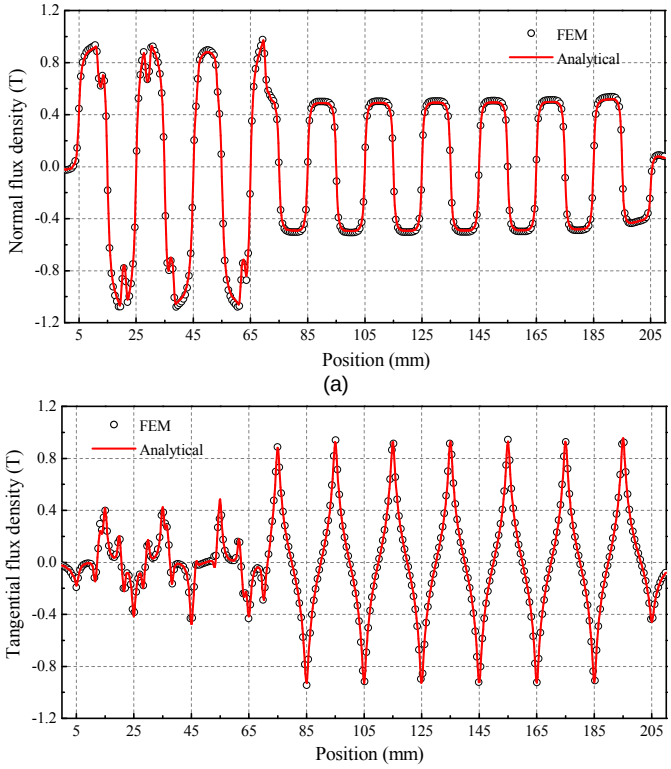

Fig. 7. Comparison of flux density at middle of the air gap when the primary iron is at the end position: (a) normal flux density, and (b) tangential flux density.

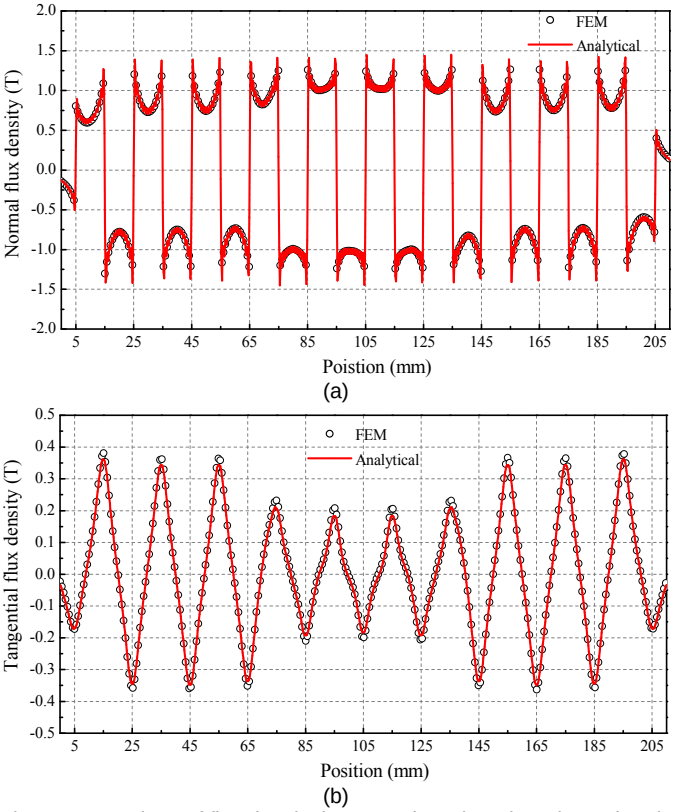

Fig. 8. Comparison of flux density in PM region when the primary iron is at the middle position: (a) normal flux density, and (b) tangential flux density.

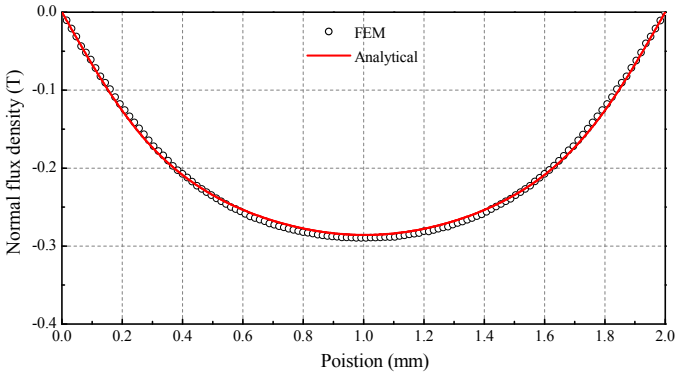

(a)

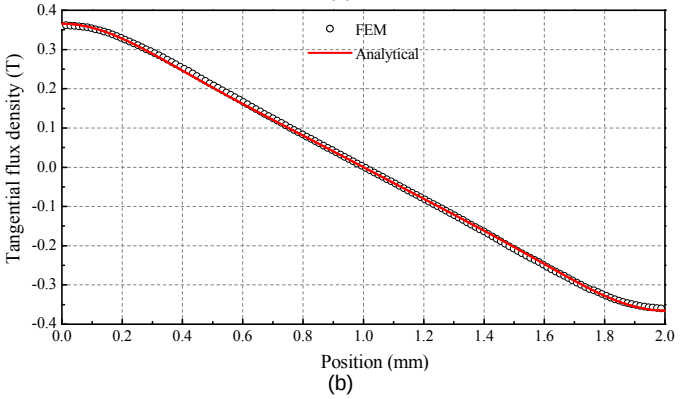

(b)

Fig. 9. Comparison of flux density in slot-opening region when the primary iron is at the middle position: (a) normal flux density, and (b) tangential flux density.

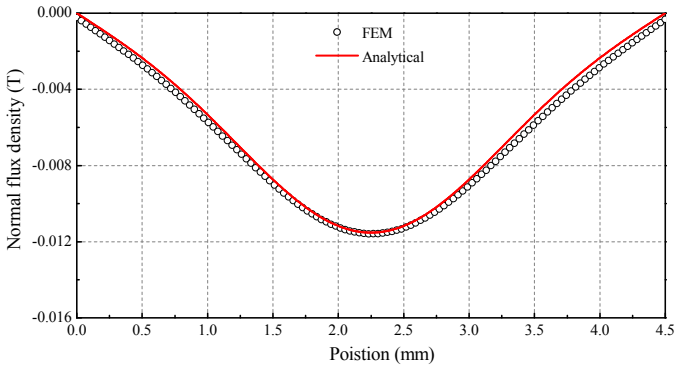

(a)

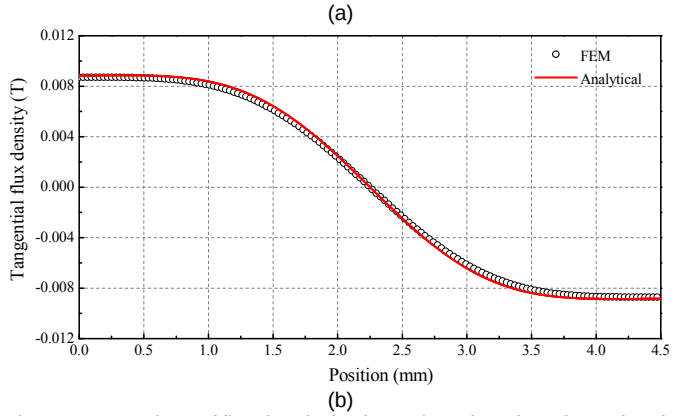

(b)

Fig. 10. Comparison of flux density in slot region when the primary iron is at the middle position: (a) normal flux density, and (b) tangential flux density.

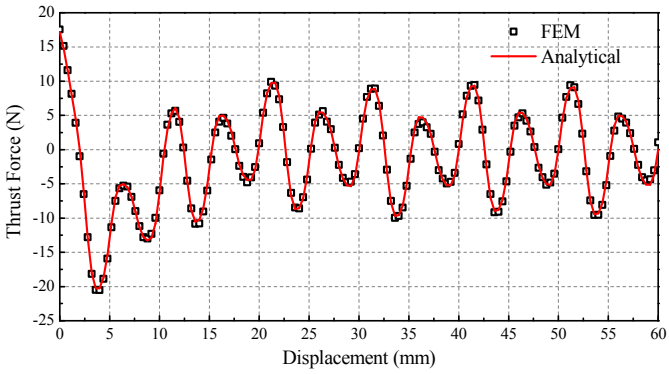

(a)

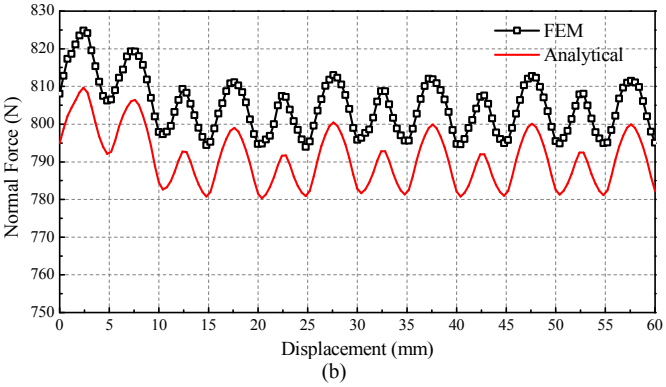

(b)

Fig. 11. Comparison of forces: (a) thrust force, and (b) normal force.

Fig. 13 compares the thrust force obtained by the analytical model, linear and nonlinear FEM models, and experimental measurement. As shown, the analytical results, linear and nonlinear FEM results and experimental results agree with each other very well. It can be seen that the magnetic nonlinearity has very little impact on the thrust force profile. The error between the theoretical and experimental results at the lower amplitudes may be attributed to lower precision of the force sensor when measuring small forces, and the magnetic nonlinearity of PMs.

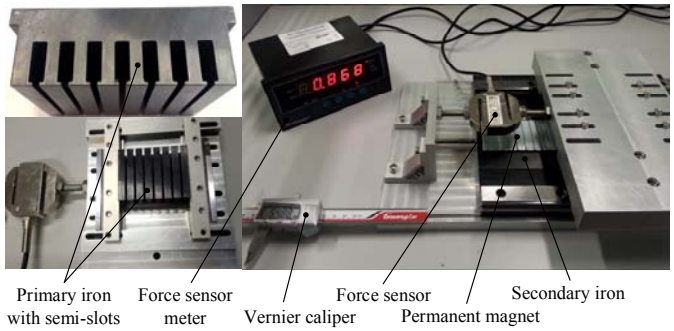

Fig. 12. The experimental testing platform for the LPMSM with semi-closed slots.

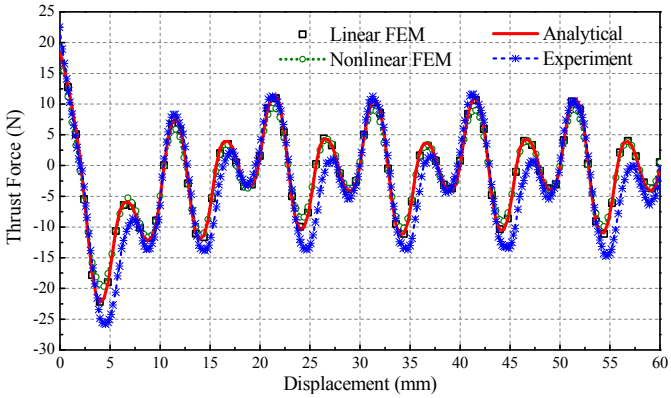

Fig. 13. Comparison of thrust force obtained by the linear and nonlinear FEM, analytical model and experimental measurement.

VI. Conclusion

In the paper, an improved SD model accounting for the slot and end effects is developed for predicting the magnetic field distribution and cogging force. Through transforming the LPMSM into an arc-linear PMSM, the magnetic field is calculated by the SD analytical model and verified by the FEM. The thrust and normal forces are further investigated which can benefit the performance optimization and dynamic modeling of LPMSMs. The analytical predictions agree well with the finite element analysis results. The maximum error is less than 2%, which may be attributed to the discretization effects of the FEM and the curvature effect of the analytical model. A prototype of the LPMSM with semi-closed slots is manufactured and tested. An excellent agreement is obtained between the calculated and experimental results. Some small errors may be attributed to the lower precision of the force sensor when measuring small forces, and the magnetic nonlinearity of PMs.

Appendix

1) Interface between Regions 1 and 2

The tangential field strength on the inner surface of the secondary back-iron is zero since the permeability of back-iron is infinite, and it is continuous along the rest part, i.e.

$$H_{\theta 1}\big|_{r=R_{ri}}=0 \quad \theta_s\in(\theta_{sr},\theta_{sr}+\theta_3)$$

$$H_{\theta 1}\big|_{r=R_{ri}}=H_{\theta 2}\big|_{r=R_{ri}} \quad \theta_s\in(\theta_{sr}+\theta_3,\theta_{sr}+\theta_3+\theta_4)$$

According to (19), (20), and (30), the following equation set can be obtained:

$$A_{1n}g_{1an}(R_{ri})=\frac{1}{\pi}\sum_{m=1}^{\infty}\left[A_{2m}g_{2am}(R_{ri})+B_{2m}g_{2bm}(R_{ri})\right]\eta_{mn}(m,n) \quad (34)$$

$$C_{1n}g_{1an}(R_{ri})=\frac{1}{\pi}\sum_{m=1}^{\infty}\left[A_{2m}g_{2am}(R_{ri})+B_{2m}g_{2bm}(R_{ri})\right]\xi_{mn}(m,n) \quad (35)$$

where

$$g_{1an}(r)=-\frac{n}{R_{ri}}\left(\frac{r}{R_{ri}}\right)^{n-1}$$

$$g_{2am}(r)=-\frac{m\pi}{\theta_4}\frac{1}{R_r}\left(\frac{r}{R_r}\right)^{\frac{m\pi}{\theta_4}-1}$$

$$g_{2bm}(r)=\frac{m\pi}{\theta_4}\frac{1}{R_{ri}}\left(\frac{r}{R_{ri}}\right)^{-\frac{m\pi}{\theta_4}-1}$$

$$\eta_{mn}=\begin{cases}\frac{\theta_4}{2}\cos n(\theta_{sr}+\theta_3)+\frac{1}{4n}\left[\cos m\pi\sin n(\theta_{sr}+\theta_3+\theta_4)-\sin n(\theta_{sr}+\theta_3)\right] & m\pi=n\theta_4\\ -\frac{n\theta_4^2}{(m\pi)^2-(n\theta_4)^2}\left[\cos m\pi\sin n(\theta_{sr}+\theta_3+\theta_4)-\sin n(\theta_{sr}+\theta_3)\right] & m\pi\neq n\theta_4\end{cases}$$

$$\xi_{mn}=\begin{cases}\frac{\theta_4}{2}\sin n(\theta_{sr}+\theta_3)-\frac{1}{4n}\left[\cos m\pi\cos n(\theta_{sr}+\theta_3+\theta_4)-\cos n(\theta_{sr}+\theta_3)\right] & m\pi=n\theta_4\\ \frac{-n\theta_4^2}{(m\pi)^2-(n\theta_4)^2}\left[\cos m\pi\cos n(\theta_{sr}+\theta_3+\theta_4)-\cos n(\theta_{sr}+\theta_3)\right] & m\pi\neq n\theta_4\end{cases}.$$

The continuous condition of radial flux density on the interface between Regions 1 and 2 is:

$$B_{1r}\big|_{r=R_{ri}}=B_{2r}\big|_{r=R_{ri}} \quad \theta_s\in(\theta_{sr}+\theta_3,\theta_{sr}+\theta_3+\theta_4)$$

According to (19), (20) and (27), the following equation can be obtained:

$$A_{2m}f_{2am}(R_{ri})+B_{2m}f_{2bm}(R_{ri})=\frac{2}{\theta_4}\sum_{n=1}^{\infty}A_{1n}f_{1an}(R_{ri})\eta_{mn}(m,n)+C_{1n}f_{1an}(R_{ri})\xi_{mn}(m,n) \quad (36)$$

2) Interface between Regions 2 and 3

The tangential field strength on the outer surface of the secondary back-iron is also zero. The continuous condition along the rest part is

$$H_{3\theta}\big|_{r=R_r}=0 \quad \theta_s\in(\theta_{sr},\theta_{sr}+\theta_3)$$

$$H_{3\theta}\big|_{r=R_r}=H_{2\theta}\big|_{r=R_r} \quad \theta_s\in(\theta_{sr}+\theta_3,\theta_{sr},\theta_{sr}+\theta_3+\theta_4)$$

According to (20), (21), and (30), the following equations can be obtained:

$$\frac{1}{\mu_r}\left[A_{3n}g_{3an}(R_r)+B_{3n}g_{3bn}(R_r)-k_{cn}(R_r)-\mu_0M_{cn\theta}\right]=\frac{1}{\pi}\sum_{m=1}^{\infty}\left[A_{2m}g_{2am}(R_r)+B_{2m}g_{2bm}(R_r)\right]\eta_{mn}(m,n) \quad (37)$$

$$\frac{1}{\mu_r}\left[C_{3n}g_{3an}(R_r)+D_{3n}g_{3bn}(R_r)-k_{sn}(R_r)-\mu_0M_{sn\theta}\right]=\frac{1}{\pi}\sum_{m=1}^{\infty}\left[A_{2m}g_{2am}(R_r)+B_{2m}g_{2bm}(R_r)\right]\xi_{mn}(m,n) \quad (38)$$

where

$$g_{3an}(r)=-\frac{n}{R_m}\left(\frac{r}{R_m}\right)^{n-1}$$

$$g_{3bn}(r)=\frac{n}{R_r}\left(\frac{r}{R_r}\right)^{-n-1}$$

$$k_{cn}(r)=\begin{cases}\frac{\mu_0(M_{c\theta n}-nM_{srn})}{n^2-1} & n\neq 1\\ -\frac{\mu_0(M_{c\theta n}-M_{srn})}{2}(\ln r+1) & n=1\end{cases}$$

$$k_{sn}(r)=\begin{cases}\frac{\mu_0(M_{s\theta n}+nM_{crn})}{n^2-1} & n\neq 1\\ -\frac{\mu_0(M_{s\theta n}+M_{crn})}{2}(\ln r+1) & n=1\end{cases}.$$

The continuous condition of radial flux density on the interface between Regions 2 and 3 is

$$B_{2r}\big|_{r=R_r}=B_{3r}\big|_{r=R_r}\quad \theta_s\in(\theta_{sr}+\theta_3,\theta_{sr}+\theta_3+\theta_4)$$

According to (20), (21), and (27), the following equation can be obtained:

$$\begin{aligned}&A_{2m}f_{2am}(R_r)+B_{2m}f_{2bm}(R_r)=\\&\frac{2}{\theta_4}\sum_{n=1}^{\infty}\Big\{\Big[A_{3n}f_{3an}(R_r)+B_{3n}f_{3bn}(R_r)+l_{cn}(R_r)\Big]\eta_{mn}(m,n)\\&+\Big[C_{3n}f_{3an}(R_r)+D_{3n}f_{3bn}(R_r)+l_{sn}(R_r)\Big]\xi_{mn}(m,n)\Big\}\end{aligned}\tag{39}$$

3) Interface between Regions 3 and 4

The continuous condition of tangential field strength on the interface between Regions 3 and 4 is

$$H_{3\theta}\big|_{r=R_m}=H_{4\theta}\big|_{r=R_m}\quad \theta_s\in(0,2\pi)$$

According to (21), (22), and (30), the following equations can be obtained:

$$\begin{aligned}&\frac{1}{\mu_r}\Big[A_{3n}g_{3an}(R_m)+B_{3n}g_{3bn}(R_m)-k_{cn}(R_m)-\mu_0M_{cn\theta}\Big]\\&\qquad=A_{4n}g_{4an}(R_m)+B_{4n}g_{4bn}(R_m)\end{aligned}\tag{40}$$

$$\begin{aligned}&\frac{1}{\mu_r}\Big[C_{3n}g_{3an}(R_m)+D_{3n}g_{3bn}(R_m)-k_{sn}(R_m)-\mu_0M_{sn\theta}\Big]\\&\qquad=C_{4n}g_{4an}(R_m)+D_{4n}g_{4bn}(R_m)\end{aligned}\tag{41}$$

where

$$g_{4an}(r)=-\frac{n}{R_s}\left(\frac{r}{R_s}\right)^{n-1}$$

$$g_{4bn}(r)=\frac{n}{R_m}\left(\frac{r}{R_m}\right)^{-n-1}.$$

The continuous condition of radial flux density on the interface between Regions 3 and 4 is

$$B_{3r}\big|_{r=R_m}=B_{4r}\big|_{r=R_m}\quad \theta_s\in(0,2\pi)$$

According to (21), (22) and (27), the following equation can be obtained:

$$\begin{aligned}&A_{3n}f_{3an}(R_m)+B_{3n}f_{3bn}(R_m)+l_{cn}(R_m)\\&\qquad=A_{4n}f_{4an}(R_m)+B_{4n}f_{4bn}(R_m)\end{aligned}\tag{42}$$

$$\begin{aligned}&C_{3n}f_{3an}(R_m)+D_{3n}f_{3bn}(R_m)+l_{sn}(R_m)\\&\qquad=C_{4n}f_{4an}(R_m)+D_{4n}f_{4bn}(R_m)\end{aligned}\tag{43}$$

4) Interfaces between Regions 4, 5, and 7j

The tangential field strength $H_{4\theta}$ is equal to $H_{5\theta}$ or $H_{7j\theta}$ on the interfaces between Regions 4 and 5, or Regions 4 and 7*j*, is zero on the surface of primary iron, i.e.

$$H_{4\theta}\big|_{r=R_s}=\begin{cases}H_{5\theta}\big|_{r=R_s} & \theta_s\in\left(\pi-\dfrac{\theta_2}{2},\pi+\dfrac{\theta_2}{2}\right)\\ H_{7j\theta}\big|_{r=R_s} & \theta_s\in\left(-\dfrac{\theta_{b0}}{2}+\theta_j,\dfrac{\theta_{b0}}{2}+\theta_j\right)\end{cases}$$

According to (22), (23), (25), and (30), the following equations can be obtained:

$$A_{4n}g_{4an}(R_s)+B_{4n}g_{4bn}(R_s)=A_{5n}^F(R_s)+A_7^F(R_s)\tag{44}$$

$$C_{4n}g_{4an}(R_s)+D_{4n}g_{4bn}(R_s)=B_{5n}^F(R_s)+B_7^F(R_s)\tag{45}$$

where

$$g_{5ak}(r)=-\frac{k\pi}{\theta_2}\frac{1}{R_{so}}\left(\frac{r}{R_{so}}\right)^{\frac{k\pi}{\theta_2}-1}$$

$$g_{5bk}(r)=\frac{k\pi}{\theta_2}\frac{1}{R_s}\left(\frac{r}{R_s}\right)^{-\frac{k\pi}{\theta_2}-1}$$

$$A_{5n}^F(r)=\frac{1}{\pi}\sum_{k=1}^{\infty}\Big[A_{5k}g_{5ak}(r)+B_{5k}g_{5bk}(r)\Big]\eta_{kn}(k,n)$$

$$B_{5n}^F(r)=\frac{1}{\pi}\sum_{k=1}^{\infty}\Big[A_{5k}g_{5ak}(r)+B_{5k}g_{5bk}(r)\Big]\xi_{kn}(k,n)$$

$$A_7^F(r)=\sum_{j=1}^{N_s}A_{7j}^F(r)=\frac{1}{\pi}\sum_{j=1}^{N_s}\sum_{u=1}^{\infty}\Big[A_{7ju}g_{7au}(r)+B_{7ju}g_{7bu}(r)\Big]\eta_{unj}(u,n)$$

$$B_7^F(r)=\sum_{j=1}^{N_s}B_{7j}^F(r)=\frac{1}{\pi}\sum_{j=1}^{N_s}\sum_{u=1}^{\infty}\Big[A_{7ju}g_{7au}(r)+B_{7ju}g_{7bu}(r)\Big]\xi_{unj}(u,n)$$

$$\eta_{kn}(k,n)=\begin{cases}\dfrac{\theta_2}{2}\cos n\left(\pi-\dfrac{\theta_2}{2}\right)+\dfrac{1}{4n}\left[\cos k\pi\sin n\left(\pi+\dfrac{\theta_2}{2}\right)-\sin n\left(\pi-\dfrac{\theta_2}{2}\right)\right] & k\pi=n\theta_2\\ \dfrac{-n\theta_2^2}{(k\pi)^2-(n\theta_2)^2}\left[\cos k\pi\sin n\left(\pi+\dfrac{\theta_2}{2}\right)-\sin n\left(\pi-\dfrac{\theta_2}{2}\right)\right] & k\pi\neq n\theta_2\end{cases}$$

$$\xi_{kn}(k,n)=\begin{cases}\dfrac{\theta_2}{2}\sin n\left(\pi-\dfrac{\theta_2}{2}\right)-\dfrac{1}{4n}\left[\cos k\pi\cos n\left(\pi+\dfrac{\theta_2}{2}\right)-\cos n\left(\pi-\dfrac{\theta_2}{2}\right)\right] & k\pi=n\theta_2\\ \dfrac{n\theta_2^2}{(k\pi)^2-(n\theta_2)^2}\left[\cos k\pi\cos n\left(\pi+\dfrac{\theta_2}{2}\right)-\cos n\left(\pi-\dfrac{\theta_2}{2}\right)\right] & k\pi\neq n\theta_2\end{cases}$$

$$\eta_{unj}=\begin{cases}\dfrac{\theta_{b0}}{2}\cos n\left(\theta_j-\dfrac{\theta_{b0}}{2}\right)+\dfrac{1}{4n}\left[\cos u\pi\sin n\left(\theta_j+\dfrac{\theta_{b0}}{2}\right)-\sin n\left(\theta_j-\dfrac{\theta_{b0}}{2}\right)\right] & u\pi=n\theta_{b0}\\ \dfrac{-n\theta_{b0}^2}{(u\pi)^2-(n\theta_{b0})^2}\left[\cos u\pi\sin n\left(\theta_j+\dfrac{\theta_{b0}}{2}\right)-\sin n\left(\theta_j-\dfrac{\theta_{b0}}{2}\right)\right] & u\pi\neq n\theta_{b0}\end{cases}$$

$$\xi_{unj}=\begin{cases}\dfrac{\theta_{b0}}{2}\sin n\left(\theta_j-\dfrac{\theta_{b0}}{2}\right)-\dfrac{1}{4n}\left[\cos u\pi\cos n\left(\theta_j+\dfrac{\theta_{b0}}{2}\right)-\cos n\left(\theta_j-\dfrac{\theta_{b0}}{2}\right)\right] & u\pi=n\theta_{b0}\\ \dfrac{n\theta_{b0}^2}{(u\pi)^2-(n\theta_{b0})^2}\left[\cos u\pi\cos n\left(\theta_j+\dfrac{\theta_{b0}}{2}\right)-\cos n\left(\theta_j-\dfrac{\theta_{b0}}{2}\right)\right] & u\pi\neq n\theta_{b0}\end{cases}.$$

The continuous condition of radial flux density on the interface between Regions 4 and 5 is

$$B_{4r}\big|_{r=R_s}=B_{5r}\big|_{r=R_s}\quad \theta_s\in\left(\pi-\frac{\theta_2}{2},\pi+\frac{\theta_2}{2}\right)$$

According to (22), (23) and (27), the following equation can be obtained:

$$\begin{aligned}&A_{5k}f_{5ak}(R_s)+B_{5k}f_{5bk}(R_s)=\\&\frac{2}{\theta_2}\sum_{n=1}^{\infty}\Big[A_{4n}f_{4an}(R_s)+B_{4n}f_{4bn}(R_s)\Big]\eta_{kn}(k,n)\\&+\Big[C_{4n}f_{4an}(R_s)+D_{4n}f_{4bn}(R_s)\Big]\xi_{kn}(k,n)\end{aligned}\tag{46}$$

The continuous condition of radial flux density on the interface between Regions 4 and 7*j* is

$$B_{4r}\big|_{r=R_s}=B_{7jr}\big|_{r=R_s}\quad \theta_s\in\left(\theta_j-\frac{\theta_{b0}}{2},\theta_j+\frac{\theta_{b0}}{2}\right)$$

According to (22), (25) and (27), the following equation can be obtained:

$$\begin{aligned}&A_{7ju}f_{7au}(R_s)+B_{7ju}f_{7bu}(R_s)=\\&\frac{2}{\theta_{b0}}\sum_{n=1}^{\infty}\Big[A_{4n}f_{4an}(R_s)+B_{4n}f_{4bn}(R_s)\Big]\eta_{unj}(u,n)+\\&+\Big[C_{4n}f_{4an}(R_s)+D_{4n}f_{4bn}(R_s)\Big]\xi_{unj}(u,n)\quad j=1,2,\cdots,N_s\end{aligned}\tag{47}$$

5) Interface between Regions 5 and 6

The tangential field strength on the outer surface of the primary iron core is zero since the permeability of iron core is infinite, and it is continuous along the rest part, i.e.

$$H_{\theta 6}\Big|_{r=R_{so}} = \begin{cases} 0 \quad \theta_s \in \left(\pi+\dfrac{\theta_2}{2}, 2\pi\right) \cup \left(0, \pi-\dfrac{\theta_2}{2}\right) \\ H_{\theta 5}\Big|_{r=R_{so}} \quad \theta_s \in \left(\pi-\dfrac{\theta_2}{2}, \pi+\dfrac{\theta_2}{2}\right) \end{cases}$$

According to (23), (24), and (30), the following equations can be obtained:

$$B_{6n} g_{6bn}\left(R_{so}\right) = A_{5n}^{F}\left(R_{so}\right) \tag{48}$$

$$D_{6n} g_{6bn}\left(R_{so}\right) = B_{5n}^{F}\left(R_{so}\right) \tag{49}$$

where

$$g_{6bn}(r) = \frac{n}{R_{so}}\left(\frac{r}{R_{so}}\right)^{-n-1}.$$

The continuous condition of radial flux density on the interface between Regions 5 and 6 is

$$B_{5r}\Big|_{r=R_{so}} = B_{6r}\Big|_{r=R_{so}} \quad \theta_s \in \left(\pi-\frac{\theta_2}{2}, \pi+\frac{\theta_2}{2}\right)$$

According to (23), (24) and (27), the following equation can be obtained:

$$\begin{aligned} &A_{5k} f_{5ak}\left(R_{so}\right) + B_{5k} f_{5bk}\left(R_{so}\right) = \\ &\quad \frac{2}{\theta_2}\sum_{n=1}^{\infty} B_{6n} f_{6bn}\left(R_{so}\right)\eta_{kn}\left(k,n\right) + D_{6n} f_{6bn}\left(R_{so}\right)\xi_{kn}\left(k,n\right) \end{aligned} \tag{50}$$

6) Interface between Regions 7j and 8i

The continuous condition of tangential field strength on the interface between Regions 7*j* and 8*i* is

$$H_{7j\theta}\Big|_{r=R_{sa}} = H_{8i\theta}\Big|_{r=R_{sa}} \quad i=j \text{ and } \theta_s \in \left(-\frac{\theta_{b0}}{2}+\theta_j, \frac{\theta_{b0}}{2}+\theta_j\right)$$

According to (25), (26), and (30), the following equation can be obtained:

$$\begin{aligned} &\frac{2}{\theta_w}\sum_{u=1}^{\infty}\left[A_{7ju} f_{7au}\left(R_{sa}\right) + B_{7ju} f_{7bu}\left(R_{sa}\right)\right]\sigma_{uvj}\left(u,v\right) = \\ &\qquad A_{8jv} g_{8av}\left(R_{sa}\right) \quad j=1,2,\cdots,N_s \end{aligned} \tag{51}$$

where

$$g_{8av}(r) = -\frac{v\pi}{\theta_w}\frac{1}{R_{sb}}\left(\frac{R_{sa}}{R_{sb}}\right)^{\frac{v\pi}{\theta_w}}\left(\frac{r}{R_{sb}}\right)^{\frac{v\pi}{\theta_w}-1} + \frac{v\pi}{\theta_w}\frac{1}{R_{sa}}\left(\frac{r}{R_{sa}}\right)^{-\frac{v\pi}{\theta_w}-1}$$

$$\sigma_{uvj}(u,v) = \begin{cases} \dfrac{-\dfrac{v\pi}{\theta_w}}{\left(\dfrac{u\pi}{\theta_{b0}}\right)^2 - \left(\dfrac{v\pi}{\theta_w}\right)^2} \times \left[\cos u\pi \sin\dfrac{v\pi}{\theta_w}\left(\theta_j - \theta_i + \dfrac{\theta_{b0}}{2} + \dfrac{\theta_w}{2}\right)\right. \\ \qquad \left. -\sin\dfrac{v\pi}{\theta_w}\left(\theta_j - \theta_i + \dfrac{\theta_w}{2} - \dfrac{\theta_{b0}}{2}\right)\right] \quad \dfrac{u\pi}{\theta_{b0}} \neq \dfrac{v\pi}{\theta_w} \\ \dfrac{\theta_{b0}}{2}\cos\dfrac{u\pi}{\theta_{b0}}\left(\dfrac{\theta_{b0}}{2} - \theta_j - \dfrac{\theta_w}{2} + \theta_i\right) + \dfrac{\theta_{b0}}{4u\pi}\left[\cos u\pi \times\right. \\ \qquad \left. \sin\dfrac{v\pi}{\theta_w}\left(\theta_j - \theta_i + \dfrac{\theta_{b0}}{2} + \dfrac{\theta_w}{2}\right) - \sin\dfrac{v\pi}{\theta_w}\left(\theta_j - \theta_i + \dfrac{\theta_w}{2} - \dfrac{\theta_{b0}}{2}\right)\right] \quad \dfrac{u\pi}{\theta_{b0}} = \dfrac{v\pi}{\theta_w} \end{cases}$$

The continuous condition of radial flux density on the interface between Regions 7*j* and 8*i* is

$$B_{7jr}\Big|_{r=R_{sa}} = B_{8ir}\Big|_{r=R_{sa}} \quad i=j \text{ and } \theta_s \in \left(-\frac{\theta_{b0}}{2}+\theta_j, \frac{\theta_{b0}}{2}+\theta_j\right)$$

According to (25), (26), and (27), the following equation can be obtained:

$$\begin{aligned} &A_{7ju} f_{7au}\left(R_{sa}\right) + B_{7ju} f_{7bu}\left(R_{sa}\right) = \\ &\qquad \frac{2}{\theta_{b0}}\sum_{v=1}^{\infty} A_{8jv} f_{8av}\left(R_{sa}\right)\sigma_{uvj}\left(u,v\right) \quad j=1,2,\cdots,N_s \end{aligned} \tag{52}$$

Finally, by solving the multivariable equation set of (34)-(52), the integration constants can be obtained.

REFERENCES

[1] M. Y. Wang, L. Y. Li, and D. H. Pan, "Detent force compensation for PMLSM systems based on structural design and control method combination," *IEEE Trans. Ind. Electron.*, vol. 62, no. 11, pp. 6845-6854, Nov. 2015.

[2] Y. J. Kim, M. Watada, and H. Dohmeki, "Reduction of the cogging force at the outlet edge of a stationary discontinuous primary linear synchronous motor," *IEEE Trans. Magn.*, vol. 43, no. 1, pp. 40-45, Jan. 2007.

[3] R. W. Cao, M. Cheng, C. C. Mi, and W. Hua, "Influence of leading design parameters on the force performance of a complementary and modular linear flux-switching permanent-magnet motor," *IEEE Trans. Ind. Electron.*, vol. 61, no. 5, pp. 2165-2175, May 2014.

[4] N. R. Tavana, A. Shoulaie, and V. Dinavahi, "Analytical modeling and design optimization of linear synchronous motor with stair-step-shaped magnetic poles for electromagnetic launch applications," *IEEE Trans. Plasma Sci.*, vol. 40, no. 2, pp. 519-527, Feb. 2012.

[5] F. Cupertino, P. Giangrande, G. Pellegrino, and L. Salvatore, "End effects in linear tubular motors and compensated position sensorless control based on pulsating voltage injection," *IEEE Trans. Ind. Electron.*, vol. 61, no. 5, pp. 2208-2216, May 2014.

[6] J. B. Wang, G. W. Jewell, and D. Howe, "Analytical framework for thrust enhancement in permanent-magnet (PM) linear synchronous motors with segmented PM poles," *IEEE Trans. Magn.*, vol. 35, no. 3, pp. 1986-2000, May. 1999.

[7] N. Bianchi, "Analytical field computation of a tubular permanent-magnet linear motor," *IEEE Trans. Magn.*, vol. 36, no. 5, pp. 3798-3801, Sep. 2000.

[8] B. L. J. Gysen, E. A. Lomonova, J. J. H. Paulides, and A. J. A. Vandenput, "Analytical and numerical techniques for solving Laplace and Poisson equations in a tubular permanent-magnet actuator: part I. semi-analytical framework," *IEEE Trans. Magn.*, vol. 44, no. 7, pp. 1751-1760, July 2008.

[9] G. H. Kang, J. P. Hong, and G. T. Kim, "A novel design of an air-core type permanent magnet linear brushless motor by space harmonics field analysis," *IEEE Trans. Magn.*, vol. 37, no. 5, pp. 3732-3736, Sep. 2001.

[10] K. J. W. Pluk, J. W. Jansen, and E. A. Lomonova, "Force measurements on a shielded coreless linear permanent magnet motor," *IEEE Trans. Magn.*, vol. 50, no. 11, 8500404, Nov. 2014.

[11] L. Yan, L. Zhang, Z. X. Jiao, H. J. Hu, C. Y. Chen, and I-Ming Chen, "Armature reaction field and inductance of coreless moving-coil tubular linear machine," *IEEE Trans. Ind. Electron.*, vol. 61, no. 12, pp. 6956-6965, Dec. 2014.

[12] S. Vaez-Zadeh and A. H. Isfahani, "Enhanced modeling of linear permanent-magnet synchronous motors," *IEEE Trans. Magn.*, vol. 43, no. 1, pp. 33-39, Jan. 2007.

[13] X. Chen and Z. Q. Zhu, "Analytical determination of optimal split ratio of E-core permanent magnet linear oscillating actuators," *IEEE Trans. Ind. Appl.*, vol. 47, no. 1, pp. 25-33, Jan./Feb. 2011.

[14] O. Danielsson and M. Leijon, "Flux distribution in linear permanent-magnet synchronous machines including longitudinal end effects," *IEEE Trans. Magn.*, vol. 43, no. 7, pp.3197-3201, July 2007.

[15] C. Pompermaier, K. F. J. Haddad, A. Zambonetti, M. V. Ferreira da Luz, and I. Boldea, "Small linear PM oscillatory motor: magnetic circuit modeling corrected by axisymmetric 2-D FEM and experimental characterization," *IEEE Trans. Ind. Electron.*, vol. 59, no. 3, pp. 1189-1196, Mar. 2012.

[16] B. Sheikh-Ghalavand, S. Vaez-Zadeh, and A. Hassanpour Isfahani, "An improved magnetic equivalent circuit model for iron-core linear permanent-magnet synchronous motors," *IEEE Trans. Magn.*, vol. 46, no. 1, pp.112-120, Jan. 2010.

[17] A. Souissi, M. W. Zouaghi, I. Abdennadher, and A. Masmoudi, "MEC-based modeling and sizing of a tubular linear PM synchronous machine," *IEEE Trans. Ind. Appl.*, vol. 51, no. 3, pp. 2181-2194, May/June 2015.

[18] P. Jin, S. H. Fang, H. Y. Lin, Z. Q. Zhu, Y. K. Huang, and X. B. Wan, "Analytical magnetic field analysis and prediction of cogging force and torque of a linear and rotary permanent magnet actuator," *IEEE Trans. Magn.*, vol. 47, no. 10, pp.3004-3007, Oct. 2011.

[19] B. L. J. Gysen, E. A. Lomonova, J. J. H. Paulides, and A. J. A. Vandenput, "Analytical and numerical techniques for solving Laplace and Poisson equations in a tubular permanent magnet actuator: part II. Schwarz–Christoffel mapping," *IEEE Trans. Magn.*, vol. 44, no. 7, pp.1761-1767, July 2007.

[20] L. Z. Zeng, X. D. Chen, X. Q. Li, W. Jiang, and X. Luo, "A thrust force analysis method for permanent magnet linear motor using Schwarz-Christoffel mapping and considering slotting effect, end effect, and magnet shape," *IEEE Trans. Magn.*, vol. 51, no. 9, article 8107609, Sep. 2015.

[21] J. B. Wang, D. Howe, and G. W. Jewell, "Fringing in tubular permanent-magnet machines: part I. magnetic field distribution, flux linkage, and thrust force," *IEEE Trans. Magn.*, vol. 39, no. 6, pp. 3507-3516, Nov. 2003.

[22] Y. Amara and G. Barakat, "Analytical modeling of magnetic field in surface mounted permanent-magnet tubular linear machines," *IEEE Trans. Magn.*, vol. 46, no. 11, pp. 3870-3884, Nov. 2010.

[23] Y. Amara, G. Barakat, and P. Reghem, "Armature reaction magnetic field of tubular linear surface-inset permanent-magnet machines," *IEEE Trans. Magn.*, vol. 47, no. 4, pp. 805-811, Nov. 2011.

[24] T. T. Overboom, J. P. C. Smeets, J. W. Jansen, and E. A. Lomonova, "Semianalytical calculation of the torque in a linear permanent-magnet motor with finite yoke length," *IEEE Trans. Magn.*, vol. 48, no. 11, pp. 3575-3578, Nov. 2012.

[25] Z. Q. Zhu, D. Howe, E. Bolte, and B. Ackermann, "Instantaneous magnetic field distribution in brushless permanent magnet dc motors, part I: open-circuit field," *IEEE Trans. Magn.*, vol. 29, no. 1, pp. 124-135, Jan. 1993.

[26] D. Zarko, D. Ban, and T. A. Lipo, "Analytical solution for cogging torque in surface permanent-magnet motors using conformal mapping," *IEEE Trans. Magn.*, vol. 44, no.1, pp. 52-65, Jan. 2008.

[27] Y. Zhou, H. S. Li, G. W. Meng, S. Zhou, and Q. Cao, "Analytical calculation of magnetic field and cogging torque in surface-mounted permanent-magnet accounting for any eccentric rotor shape," *IEEE Trans. Ind. Electron.*, vol. 62, no. 6, pp. 3438-3447, Jun. 2015.